iScience

CellPress
OPEN ACCESS

Article

Steerable mass transport in a photoresponsive system for advanced anticounterfeiting

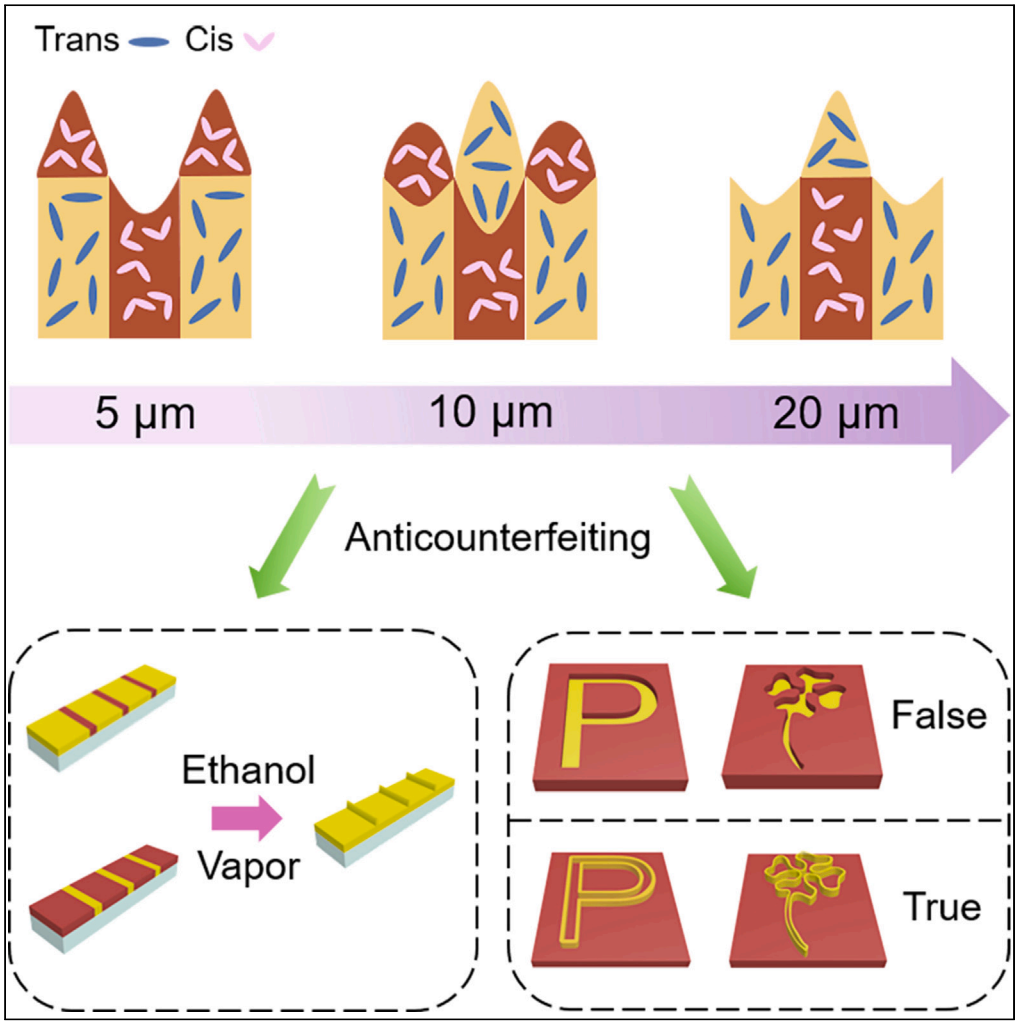

Yufan Ji, Bowen Yang, Feng Cai, Tianfu Song, Haifeng Yu

tfsong@pku.edu.cn (T.S.)
yuhaifeng@pku.edu.cn (H.Y.)

Highlights

Steerable mass transport in solvent vapor

Flow in both directions exists simultaneously under specific conditions

Multi-mode anticounterfeiting platform using controllable flow

Ji et al., iScience 27, 108790
February 16, 2024
https://doi.org/10.1016/j.isci.2024.108790

iScience

CellPress
OPEN ACCESS

Article

Steerable mass transport in a photoresponsive system for advanced anticounterfeiting

Yufan Ji,[1] Bowen Yang,[1] Feng Cai,[1] Tianfu Song,[1,*] and Haifeng Yu[1,2,*]

SUMMARY

Numerous anticounterfeiting platforms using photoresponsive materials have been designed to improve information security, enabling applications in anticounterfeiting technology. However, fabricating sophisticated micro/nanostructures using bidirectional mass transport to achieve advanced anticounterfeiting remains challenging. Here, we propose one strategy to achieve steerable mass transport in a photoresponsive system with the assistance of solvent vapor at room temperature. Upon optimizing the host-guest ratio and the width of photoisomerized areas, wettability gradient is acquired just photo-patterning once, then bidirectional mass transport is realized due to the competition of mass transport induced by surface energy gradient of the material itself and flow of the solvent on the film surface with wettability gradient. Taking advantage of the interaction between solvent and film surface with wettability gradient, this bidirectional polymer flow has been successfully applied in multi-mode anticounterfeiting. This work paves a promising avenue toward high-level information storage in soft materials, demonstrating the potential applications in anticounterfeiting.

INTRODUCTION

Directional mass transport of matter has been attached to great importance for its wide range of applications in microfluidics,[1,2] cargo transportation,[3] robotics,[4,5] etc. Recent work has demonstrated that a spontaneous, rapid mass transport is accessible on surfaces with topography gradient,[6–8] surface tension,[9,10] or surface charge density.[11] In these studies, the driving force for mass transport originates from the gradient imposed by the surface,[12,13] while the most studied is to manipulate the flow induced by surface energy gradient of polymer itself,[14–17] resulting in various micro/nanostructures for fabricating delicate patterns to achieve information encryption.[18,19] Currently, the applications of photochromic and photoluminescent materials in anticounterfeiting have been widely investigated,[20–23] and most of them focus on the color tunability,[24–26] whether reflection or photoluminescent color. However, manipulation of bidirectional polymer flow on the film surface at room temperature to fabricate micro/nanostructures for advanced anticounterfeiting is extremely important, yet rarely reported before.

Taking advantage of photoresponsive materials to modulate their physiochemical properties, especially the glass-transition temperature (T_g) and the surface energy, has been attracting great interests.[27–30] Combining with the periodic variation of these properties that is directed by photo-patterning can result in the formation of micro/nanostructures on film surface.[31–34] A typical example is azopolymer,[35] which can undergo *trans*-cis photoisomerization, leading to variation in T_g and surface energy. With the assistance of a photomask, the photo-patterned film will generate a gradient of surface energy, then heating the film can lead to a polymer flow named Marangoni flow, which is a kind of interfacial turbulence,[36] namely, an interfacial agitation driven by local variations of interfacial tension.[37] This thermally induced Marangoni flow is usually unidirectional, and a selectable direction cannot be acquired accordingly. Moreover, even though using different photochemical reactions can change the local surface tension,[38] it is still difficult to achieve a tunable direction by just patterning once at room temperature.

To solve this problem, flow of the solvent on the film surface has been introduced.[39–41] Since liquid prefers to flow from the high surface-energy region to the low surface-energy region and the flowing solvent can drag the underlying polymer to transport, thus providing a flow in the opposite direction of the thermally induced Marangoni flow for the polymer, which has been reported in our latest work.[42,43] However, T_g of that azopolymer is too high, so the Marangoni flow of azopolymer itself is unable to happen at room temperature and heat is required to trigger the flow. In this paper, we report one concise strategy to achieve well-controlled bidirectional mass transport on one film surface in solvent vapor at room temperature. By combining the Marangoni flow induced by surface energy gradient of the azopolymer itself with the capillary flow caused by the flow of the solvent on the film surface with wettability gradient, the direction of flow is steerable under certain conditions. To decrease the T_g of the system, one small-molecular liquid crystal (5CB) is introduced into the azopolymer to build a photoresponsive host-guest system (Figure 1A), then the surface deformation can be manipulated according to the host-guest ratio. Interestingly, optimization of the host-guest ratio can provide the possibility of two opposite directions of mass transport existing in the same film by

[1]School of Materials Science and Engineering, Key Laboratory of Polymer Chemistry and Physics of Ministry of Education, Peking University, Beijing 100871, China
[2]Lead contact
*Correspondence: tfsong@pku.edu.cn (T.S.), yuhaifeng@pku.edu.cn (H.Y.)
https://doi.org/10.1016/j.isci.2024.108790

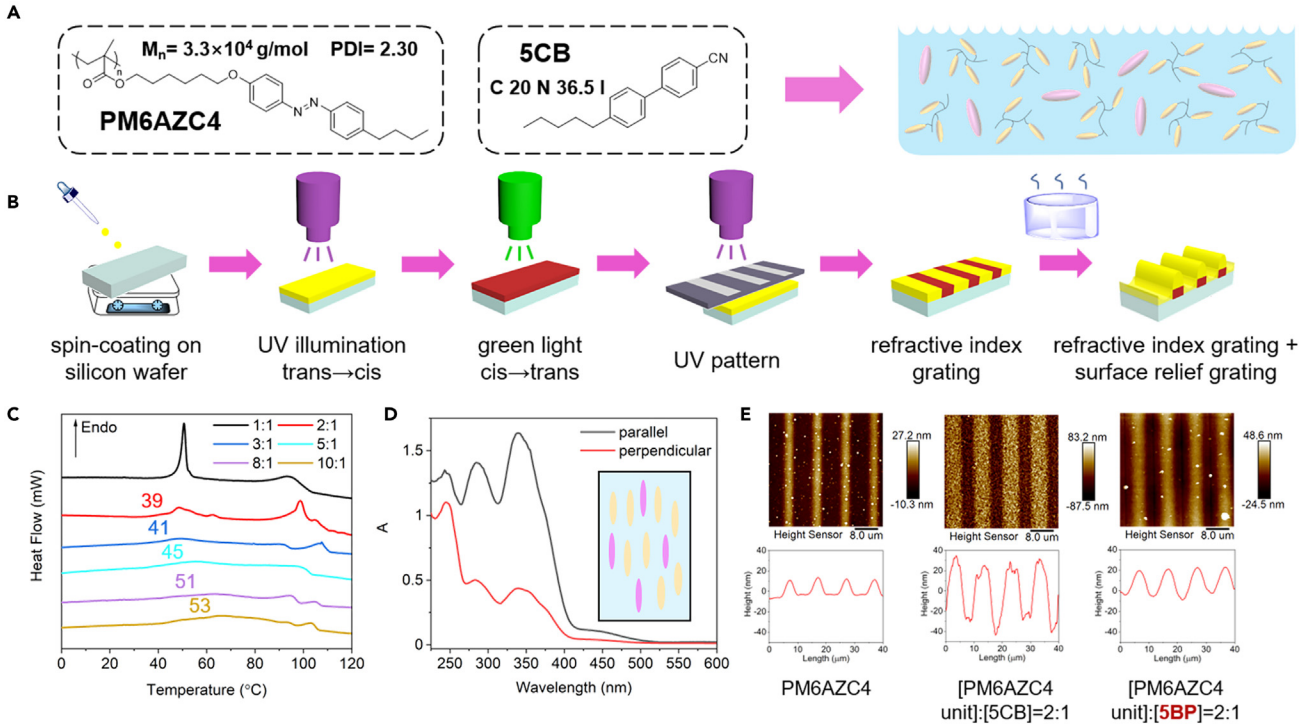

Figure 1. Chemical structures, schematic illustrations, and basic characterizations of the micro/nanostructures fabricated on the film surface

(A) Chemical structures of PM6AZC4 and 5CB and schematic diagram of the solution of the mixture.

(B) Schematic illustration of fabricating micro/nanostructures on the film surface.

(C) DSC curves of PM6AZC4 with different doping amounts of 5CB.

(D) Polarized UV spectra of the [2:1] film after photoalignment.

(E) Atomic force microscopy (AFM) images and cross-sectional profiles of the pristine PM6AZC4 film, [PM6AZC4 unit]:[5CB] = 2:1 film, and [PM6AZC4 unit]:[5BP] = 2:1 film after being sealed in the container filled with ethanol vapor for 45 min. See also Figures S1–S5.

just photo-patterning once, while the direction is determined by the width of the selectively photoisomerized region. Furthermore, multi-mode anticounterfeiting is achieved by tailoring the bidirectional flow, since the obtained micro/nanostructures are far different from the conventional ones generated by unidirectional polymer flow. These results represent a significant step in manipulation of mass transport direction and inspire a plethora of innovations for applications in anticounterfeiting using photoresponsive host-guest system.

RESULTS AND DISCUSSION

Design of the host-guest system

As shown in Figure 1A, one liquid-crystalline polymer, poly(6-(4-((4-butylphenyl) diazenyl)-phenoxy) hexyl methacrylate) (PM6AZC4) was used in this study, and its characterizations are given in Figures S1 and S2. One commercially available nematic liquid crystal, 4-cyano-4′-pentylbiphenyl (5CB) was used as a functional additive in PM6AZC4 with different molar ratios of the repeating unit of PM6AZC4 to 5CB ([PM6AZC4 unit]:[5CB]), then a host-guest system was built.

Figure 1B illustrates the stepwise process for fabricating micro/nanostructures on the film surface. First, one tetrahydro-furan (THF) solution of PM6AZC4 and 5CB was spin-coated on silicon wafers. Upon THF evaporation, the film was pre-treated with photo irradiation of UV light (365 nm) and then visible light (530 nm) (Figure S3). Subsequently, photo-patterning with a photomask was carried out to produce a surface energy gradient. Then a refractive-index grating was observed, and the surface morphing was negligible if there was no assistance of the solvent or heating. After being sealed in the container filled with ethanol vapor for a period of time, micro/nanostructures on film surface were produced. Compared to pristine PM6AZC4, the addition of 5CB enhanced the surface morphing by a large amount because it changed the thermodynamic properties of the system. In the differential scanning calorimetry (DSC) test, PM6AZC4 with different doping amounts of 5CB has different T_gs. As shown in Figure 1C, with a changing molar ratio of [PM6AZC4 unit]:[5CB] from 10:1 to 2:1, T_g decreased from 53°C to 39°C and no phase separation appeared, where 5CB and PM6AZC4 should be mixed homogeneously at the molecular level. While the [1:1] sample is unique, no T_g can be observed, but two clearing points are evident, indicating that PM6AZC4 and 5CB were immiscible at this ratio (DSC curves of pure PM6AZC4 and 5CB are given in Figure S4). Obviously, 5CB may act as a plasticizer when there is no phase separation in a broad host-guest ratio, which helps increasing the mobility of polymer and contributes to enhanced surface deformation.

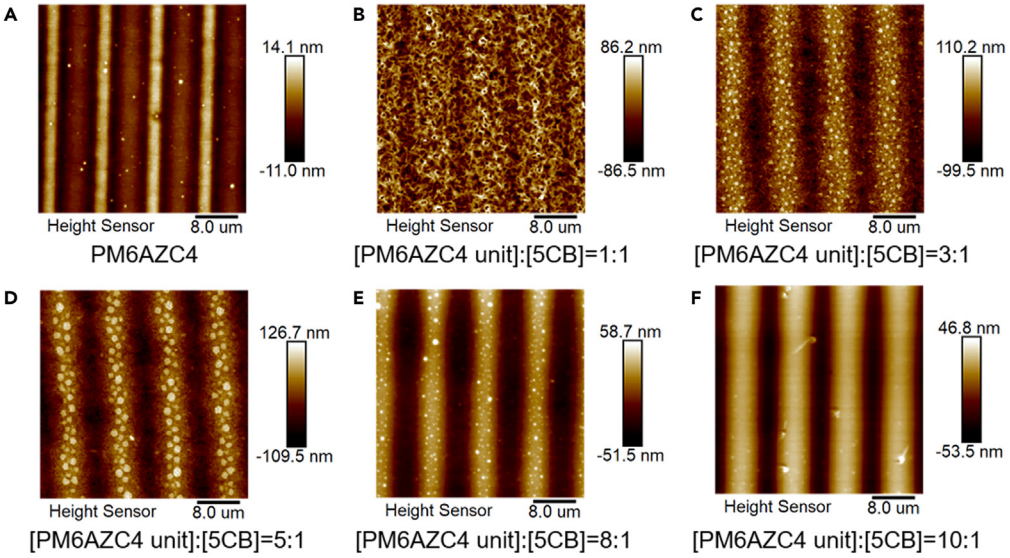

Figure 2. The response to methanol vapor of the films with different host-guest ratios

AFM images of (A) the pristine PM6AZC4 film, (B) the [1:1] film, (C) the [3:1] film, (D) the [5:1] film, (E) the [8:1] film, (F) the [10:1] film after being sealed in the container filled with methanol vapor for 45 min. See also Figures S6–S8.

More importantly, the molecular cooperative motion between 5CB and azobenzene mesogens could boost this effect.[44] Take the [2:1] film as an example, PM6AZC4 was photo-aligned perpendicularly to the polarization direction of polarized 460 nm light (Figure S5), following the Wiegert effect, and the dopant 5CB was also oriented consistently with the photoalignment direction, as indicated by polarized UV-vis absorption spectra (Figure 1D). The molecular cooperative motion in the surface morphing was further demonstrated by replacing 5CB with one non-mesogenic compound, 4-pentylbiphenyl (5BP).[45] As shown in Figure 1E, after ethanol vapor fumigation, the surface morphing of 5BP-doped film was far smaller than that of 5CB-doped film, and the mass transport was not significantly increased compared with pure PM6AZC4, further highlighting the importance of adding small-molecular liquid crystal 5CB. Therefore, it is not only the reduced T_g but also the molecular cooperative motion that enables the dopant 5CB to significantly enhance the surface morphing upon promoting the mass transport.

Mass transport in methanol vapor

The 5CB-induced enhancement of surface deformation in the host-guest system was further explored in various solvent vapors, not limited to ethanol. As shown in Figure S6, other solvents like methanol, n-hexane, and petroleum ether exhibit similar enhancement. Then the influence of host-guest ratio on the modulation of surface deformation was studied. With increasing the doping amount of 5CB, surface morphing was gradually increased upon exposure to methanol vapor (Figures 2 and S7B). However, too much 5CB lead to a macroscopic phase separation, resulted in a rough surface profile (Figure S7A) so that it was difficult to distinguish between the indentations and protrusions in the AFM image of the [1:1] sample (Figure 2B), since the boundary between the peak and valley tended to be blurred. This is unbeneficial to improving the feature height. Obviously, the [5:1] sample exhibited the best enhancement of the surface morphing (Figures 2D and S7B). Moreover, the surface deformation of samples with different host-guest ratios after being immersed in methanol was also investigated. As shown in Figure S8, periodic micro/nanostructures can also be obtained after being immersed in methanol, but there are many holes in the film since the 5CB in the film has been partially dissolved in methanol when there is a direct contact between methanol and the film. Therefore, to avoid the solvent immersion that leads to variation in the host-guest ratio of the film and generates holes that disrupt the original periodic surface morphing, solvent vapors were used in our studies.

Raman experiments of the host-guest system were performed to verify the distribution of *trans* and cis isomers upon methanol vapor fumigation and the direction of mass transport for PM6AZC4 and 5CB. As shown in Figure 3A, after pre-illumination and photo-patterning, the [5:1] film exhibited a periodic distribution of *trans* and cis isomers, where the red region (the value of scale bar ≥ 0.1) represents cis isomers and the blue/green region (the value of scale bar ≤ 0.06) represents *trans* isomers (Figures S9A and S9B), respectively. The N=N stretching vibration of cis isomers at about 1,470 cm^{-1} is a characteristic peak,[46,47] which is absent in trans isomers. Then we choose the peak at about 1,600 cm^{-1} as the characteristic peak of 5CB because it is the most evident in the Raman spectra (Figure S9C). Due to the small doping amount of 5CB, the peak intensity at around 1,600 cm^{-1} in the [5:1] film is weak, whether the unexposed or exposed areas (Figure 3A). After methanol vapor fumigation, the value of the scale bar in all regions was decreased, indicating that the mass transport direction is from *trans*-rich to *cis*-rich regions. This resulted in a mixed state of cis and *trans* isomers in the exposed area so the value of the scale bar is lower, while in the unexposed area, the *trans* isomers flowed out, also leading to a lower value of the scale bar, but the periodic distribution still remained (Figure 3B). Compared

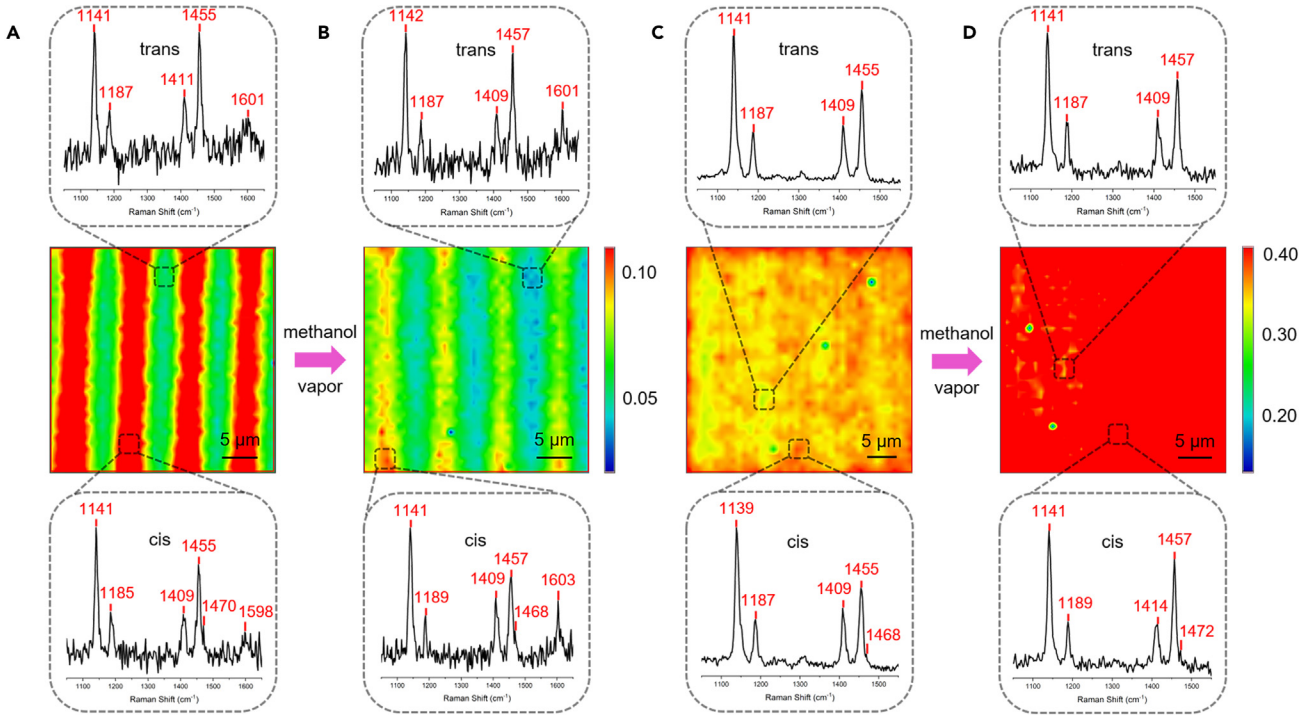

Figure 3. Raman measurements and the corresponding mapping data showing the distribution of *trans* and cis isomers in the film and the direction of mass transport for PM6AZC4 and 5CB

The [5:1] film (A) before and (B) after methanol vapor fumigation. The pure PM6AZC4 film (C) before and (D) after methanol vapor fumigation. See also Figures S9 and S10.

to previous work,[32] the flow direction is consistent with Marangoni flow of azopolymer itself. Moreover, the peak intensity at around 1,600 cm^{-1} in the exposed area raised significantly and was higher than that in the unexposed area, indicating that 5CB also flowed to the exposed area along with the mass transport of PM6AZC4 during vapor fumigation (Figure 3B). Interestingly, the pure PM6AZC4 film exhibited completely different behaviors. As shown in Figures 3C, 3D, and S10, the value of the scale bar in all regions increased after methanol vapor fumigation, demonstrating that the cis isomers appeared in the whole film plane, which should be caused by the flow of the solvent on the film surface with wettability gradient, dragging the underlying *cis*-rich polymer with lower T_g to transport. Therefore, the direction of polymer flow is consistent with the flow of the solvent on the film surface, which is different from the Marangoni flow of azopolymer itself.

Mechanism of mass transport

To further determine the flowing direction and the driving force of mass transport, photomasks consisting of transparent or opaque single stripe with different widths were used to pattern the [5:1] sample. As a result, the polymer flow in the [5:1] film was always from *trans*-rich region to *cis*-rich region whether the solvent was methanol, ethanol, or n-hexane, which is consistent with the Raman data (Figure S11). Additionally, contact-angle of the [5:1] film decreased when the *trans*-cis isomerization happens (Figures S12A–S12D), indicating that *cis* isomer possesses a higher surface tension. The surface energy of the different regions in the [5:1] film can be obtained by using the Fowkes method based on Young-Laplace equation[48]: *trans*-rich region was 36.1 mJ m^{-2} and *cis*-rich region was 43.2 mJ m^{-2}. These calculation results strongly confirmed that the direction of flow in the [5:1] film was from low surface-energy region to high surface-energy region, that is, the Marangoni flow of the azopolymer itself happened. Correspondingly, the surface energy of the different regions in the pure PM6AZC4 film was calculated using the same method (Figures S12E–S12H): *trans*-rich region was 37.7 mJ m^{-2} and *cis*-rich region was 40.9 mJ m^{-2}. According to previous work,[42] solvent on the film surface flows from high surface-energy region to low surface-energy region, that is, from *cis*-rich region to *trans*-rich region, therefore the direction of polymer flow in the pure PM6AZC4 film should also be from *cis*-rich region to *trans*-rich region.

Since the direction of polymer flow in the [5:1] film is opposite to pure PM6AZC4 film, the effect of the host-guest ratio on the direction of mass transport was explored in detail. For the [8:1] and [10:1] films with a lower molar ratio of 5CB, the direction of mass transport was the same as the [5:1] film regardless of the width or the transparency of the single stripe in the photomask when exposure to ethanol vapor (Figures S13 and S14). Amazingly, by decreasing the doping amount of 5CB to 15:1, the situation became intricate (Figure 4). When the width of the selectively photoisomerized area was 5 μm, polymer flow was from *cis*-rich region to *trans*-rich region, while for the 20 μm width, the direction was completely opposite. Then for the 10 μm width, polymer flow in both directions existed at the same time, indicating that the direction of the

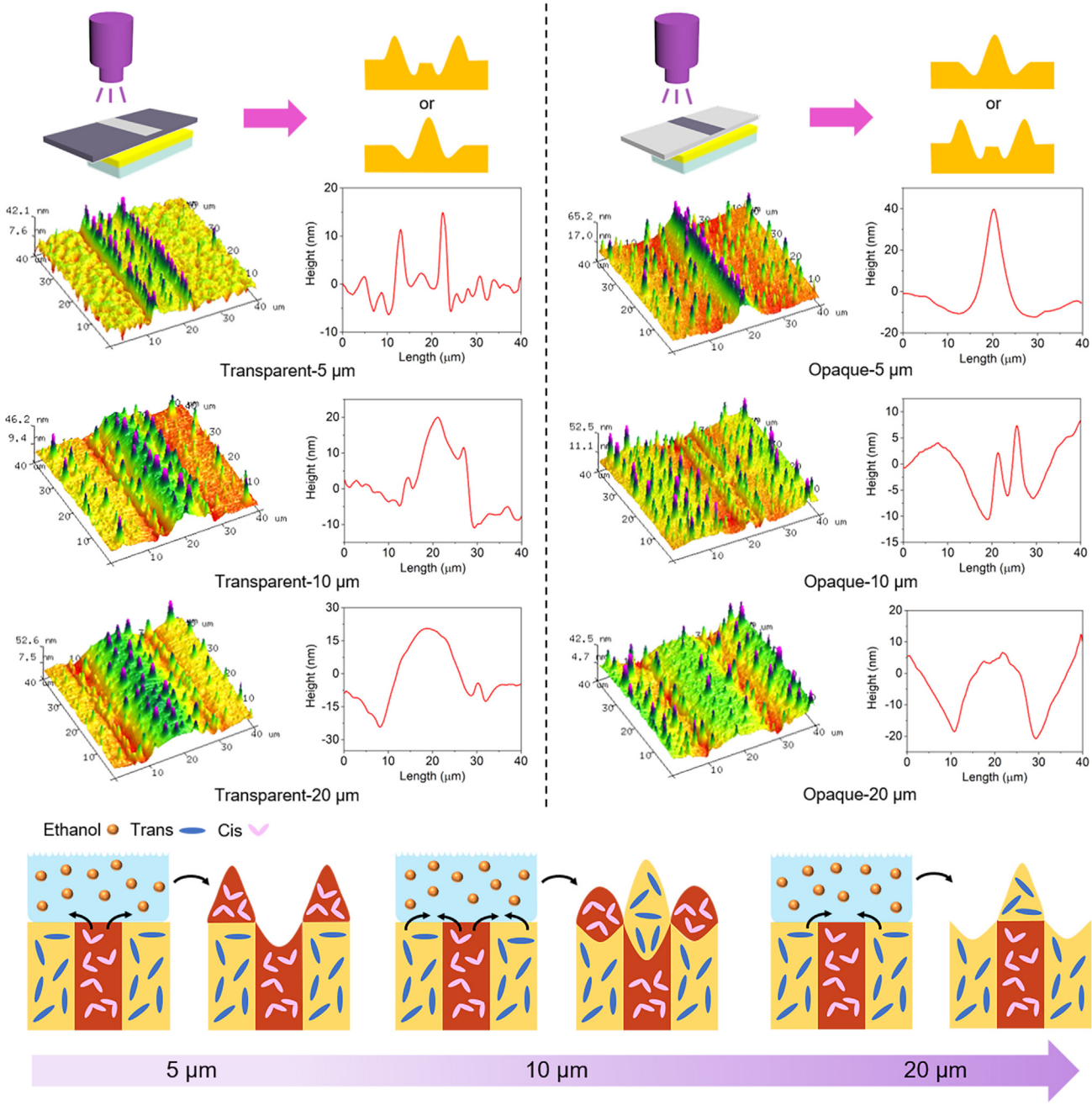

Figure 4. The direction of the polymer flow of the [15:1] film in ethanol vapor

Figure360▷ For a Figure360 author presentation of this figure, see https://doi.org/10.1016/j.isci.2024.108790.

From top to bottom, AFM images and cross-sectional profiles of the micro/nanostructures obtained by using a photomask with a single stripe where the width is 5 μm, 10 μm, and 20 μm, respectively. The single stripe used in the left part is transparent, while in the right part is opaque. The direction is from *cis*-rich to *trans*-rich area when the width is 5 μm, while the direction is opposite when the width is 20 μm. As for 10 μm, polymer flow in both directions exists at the same time. See also Figures S11–S18.

polymer flow could be manipulated by adjusting the width of the selectively photoisomerized area when the doping amount of 5CB was low enough. Furthermore, if the ethanol was substituted with other solvents, the situation was different due to the different choices of the solvent. When the methanol is used, the results are similar to that using ethanol (Figure S15). Bidirectional polymer flow happened and the direction could change with the width of the selectively photoisomerized area. However, when the solvent is n-hexane or petroleum ether, the polymer flow is unidirectional, and there is no mass transport from *cis*-rich region to *trans*-rich region (Figures S16 and S17). This is due to the fact that

non-polar solvents are unable to drag the underlying *cis*-rich polymer with higher polarity to transport, while solvents with strong polarity can. Therefore, the emergence of bidirectional polymer flow depends on the type of the solvent.

Bidirectional flow under specific conditions

This interesting bidirectional flow in the [15:1] film can be explained by comparing two kinds of polymer flow, which is induced by surface energy gradient of polymer itself and flow of the solvent on the film surface with wettability gradient, respectively. The dynamics of the polymer film can be described as follows:[15,49,50]

$$\frac{\partial h}{\partial t} + \frac{\partial}{\partial x}\left[\left(\frac{1}{2\mu}\right)h^2\frac{\partial \gamma}{\partial x} + \left(\frac{1}{3\mu}\right)h^3\frac{\partial}{\partial x}\left\{\gamma\frac{\partial^2 h}{\partial x^2}\right\}\right] = 0 \quad \text{(Equation 1)}$$

where h is the feature height of the film, γ is the surface energy of the film, μ is the viscosity, and x and t are the lateral distance and the time exposed to solvent vapor, respectively. The first part in the square bracket is the Marangoni flow, while the second one accounts for the capillary flow. Among them, Marangoni flow is resulted from the surface energy gradient of the polymer itself. Capillary flow refers to the surface morphing caused by the flow of the solvent on the film surface with wettability gradient, which is driven by the capillary force.[51,52] Here, what we are concerned about is when Marangoni flow arises and when capillary flow appears, respectively. Marangoni instability should be quantitatively characterized by a dimensionless number called "Marangoni number".[31,53,54] In Equation 2, *Ma* is defined to determine the direction of the polymer flow:

$$Ma = -\frac{\Delta\gamma L^2 \nabla c_{trans}}{\mu D} \quad \text{(Equation 2)}$$

where *Ma* is a symbol of Marangoni number, $\Delta\gamma$ is the variation in surface energy as the photoisomerization happens, L is the characteristic length of the surface energy gradient, which refers to the width of the selectively photoisomerized area in our study, ∇c_{trans} is the gradient of the content of *trans* isomers, μ has been defined in Equation 1 and D is the diffusion coefficient. The critical *Ma* is 80 according to the previous report.[31,55,56] Therefore, Marangoni flow would occur when *Ma* is over 80. If $\Delta\gamma$ and L are small, *Ma* is smaller than the critical value, then the surface energy gradient is insufficient to produce Marangoni flow, and there is only the capillary flow created by the flow of the solvent dragging the underlying polymer. When $\Delta\gamma$ or L increases, *Ma* reaches even exceeds the critical value, then Marangoni flow induced by surface energy gradient of polymer itself will arise. This is consistent with the experimental results that there are two kinds of polymer flow in the [15:1] film after being exposed to ethanol vapor. When the doping amount of 5CB is low enough (such as [15:1] film), there is a relatively small $\Delta\gamma$ in the film ($\Delta\gamma$ = 5.7 mJ m^{-2}, contact-angle data are given in Figures S12I–S12L). Therefore, when the width of the selectively photoisomerized area was 3 μm or 5 μm, mass transport happened due to the generation of capillary flow. If the selectively photoisomerized area was 15 μm width or more, only the Marangoni flow appeared. While for the 8 μm and 10 μm widths, mass transport was bidirectional (Figures 4 and S18). When the doping amount of 5CB is large enough (such as [5:1] film), $\Delta\gamma$ is large ($\Delta\gamma$ = 7.1 mJ m^{-2}, contact-angle data are given in Figures S12A–S12D), and *Ma* will exceed the critical value no matter what the L is, according to Equation 2. In this case, only the Marangoni flow exists, that is, the entire film has only one direction of flow, coinciding with the situation of the [5:1] film. If no 5CB is added (pure PM6AZC4 film), $\Delta\gamma$ is too small to generate Marangoni flow ($\Delta\gamma$ = 3.2 mJ m^{-2}, contact-angle data are given in Figures S12E–S12H), then only the capillary flow arises, which corresponds to the situation of the pure PM6AZC4 film. So far, we have realized the regulation of the direction of mass transport by tuning the parameter L when using the [15:1] film.

Applications of bidirectional flow

Generally, conventional micro/nanostructures formed by unidirectional polymer flow are easy to be duplicated. Hence, it is necessary to develop sophisticated micro/nanostructures for high-level information storage. Taking advantage of the bidirectional flow in the host-guest system, multi-mode anticounterfeiting platform was successfully designed. Specifically, the first mode is to select two photomasks to determine the authenticity of one piece of information: one has alternating 5 μm transparent width and 20 μm opaque width, and the other is just the opposite, as shown in Figure 5A. After photo-patterning, periodic distributions of *trans*-rich and *cis*-rich regions following the two photomask patterns were obtained respectively. If unidirectional flow happens upon exposure to ethanol vapor, two reversed surface topography should be acquired, indicating that the information is false. When the bidirectional polymer flow was produced as a result of tuning the width of the selectively photoisomerized area, the resulting surface topography was almost the same (Figures 5B and S19), demonstrating that the information is true. For the information written with the first photomask in the [15:1] film, Marangoni flow induced by surface energy gradient of polymer itself happened in the *trans*-rich region because the width of *trans*-rich area was 20 μm, while in the *cis*-rich region, the flow direction was opposite since the width of *cis*-rich area was 5 μm. For the information written with the other photomask, bidirectional polymer flow also existed. The result was the same in these two cases: all the flowing mass would move to the boundary of the *trans*-rich and *cis*-rich area, indicating that the information in [15:1] film is true. Furthermore, if there is only one photomask, another anticounterfeiting platform was fabricated to distinguish between two patterns that look almost identical in the microscope. As given in Figure 5C, a photomask with a three-letter pattern was utilized to pattern two films with different host-guest ratios, one is a [10:1] film, and the other is a [15:1] film. The length and width of the transparent area in the middle of the letter "P" was about 37 μm and 27 μm, respectively, while the surrounding opaque area was 8 μm width, therefore bidirectional polymer flow could happen in the [15:1] film. After ethanol vapor fumigation, two similar "PKU" patterns

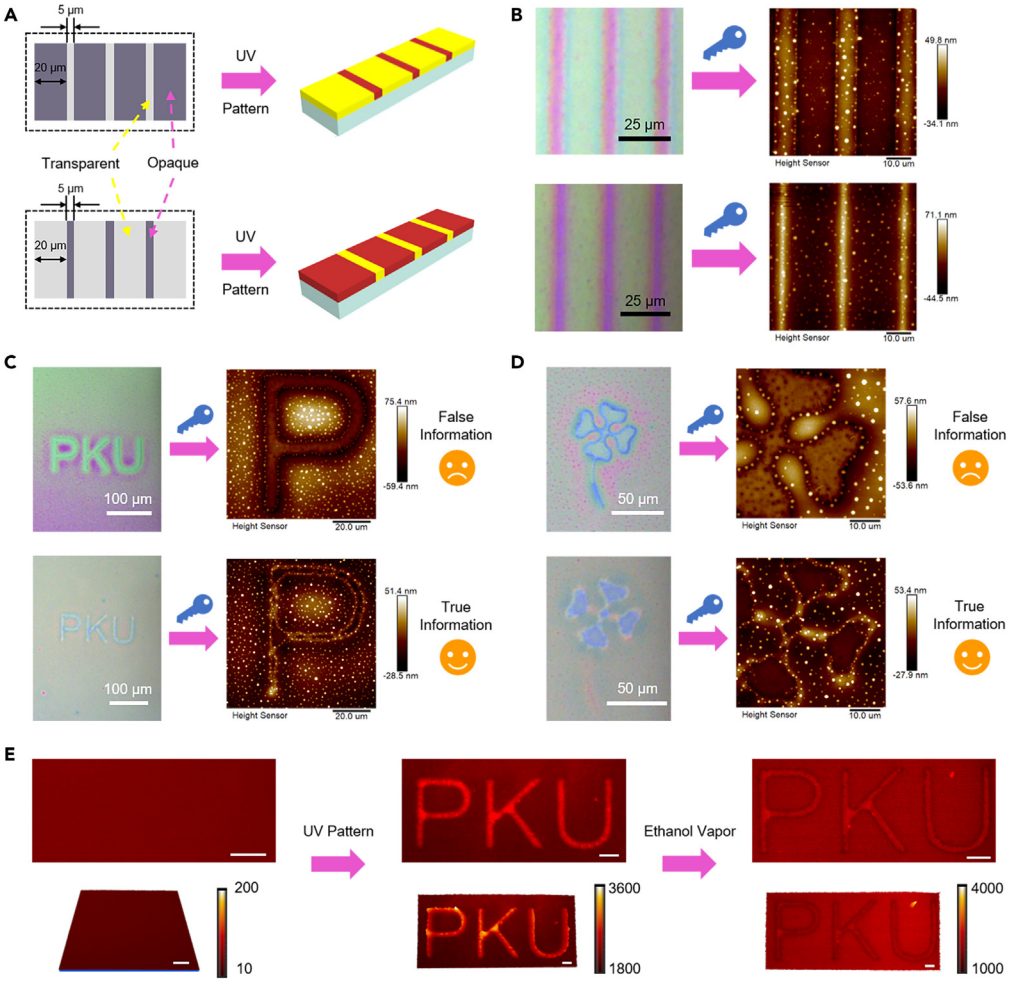

Figure 5. Applications of bidirectional polymer flow in multi-mode anticounterfeiting

(A) Schematic illustration of UV patterning using specific photomasks.

(B) Microscopic photographs and AFM images of micro/nanostructures obtained by using the photomasks in (A) and then ethanol vapor fumigation. Surface topography is almost the same, indicating the true information. Another anticounterfeiting mode using the photomask with (C) a three-letter pattern or (D) a four-leaf clover pattern, then two similar patterns can be distinguished by the difference in surface topography.

(E) Laser scanning confocal microscopy (LSCM) images and readout signal intensity mapping images of the identification process of the true information. Scale bars are all 20 μm. See also Figure S19.

can be observed by microscope (Figure 5C). To decrypt the true information, AFM measurement was carried out. In [10:1] film, polymer flow is from *trans*-rich region to *cis*-rich region and the final surface topography is caused by unidirectional flow, implying the false information. In [15:1] film, bidirectional flow happened and all the flowing mass moved to the boundary of the *trans*-rich and *cis*-rich area, leading to a raised height in the inner and outer profiles of the letter "P". This height difference is only reflected in the one-dimensional boundary, not a two-dimensional area, which is different from the [10:1] film, demonstrating the true information. Similarly, a photomask with a four-leaf clover pattern, which was irregular in shape but had an area of about 5 μm width and the adjacent area was 15 μm width or more, was used and true information could be identified in the same way with a more obvious difference between two cases (Figure 5D). Besides, the third mode for anticounterfeiting was realized. By doping a kind of red fluorescent dye Rhodamine 6G, the authenticity of the information can be identified using laser scanning confocal microscopy (LSCM) (Figure 5E). Rhodamine 6G is a small molecule and easy to be transported with the polymer flow, so polymer flow can be visualized in fluorescent images and readout signal intensity mapping images. After UV patterning using the same photomask as in Figure 5C, there is a difference in red fluorescence between the unexposed area where the three letters of "PKU" were located and other regions. If the information is true, the difference in fluorescence intensity between *trans*-rich region and *cis*-rich region will almost disappear after ethanol vapor fumigation due to the bidirectional mass transport (Figure 5E). In addition, fluorescent molecules were delivered to the *trans*-rich/*cis*-rich boundary along with the polymer flow (away from the original film plane), leading to a sharp decrease in red fluorescence intensity at the boundary in the original film plane. Therefore, true information can be identified using LSCM, providing a plethora of innovations for design of the anticounterfeiting platform.

Conclusions

Taking advantage of controllable mass transport to fabricate micro/nanostructures for anticounterfeiting is an attractive topic in materials science. In this work, we have successfully developed a facile method to achieve steerable mass transport in a host-guest system by manipulating the doping amount of 5CB and the width of the selectively photoisomerized area. The addition of 5CB enhances the mobility of the polymer chains by decreasing T_g of azopolymer and brings about amplification effect by the mesogenic molecular cooperative motion. The direction of mass transport was characterized by Raman experiments and AFM tests, while the mechanism was indicated by contact-angle measurement and surface energy calculation. Upon tuning the doping amount of 5CB and the width of the transparent/opaque area in the photomask, bidirectional flow was obtained upon exposure to solvent vapor, resulting in unique micro/nanostructures, far different from those obtained by the flow in one single direction. Therefore, multi-mode anticounterfeiting was realized. First, the authenticity of the information can be determined using two specific photomasks; second, two similar pieces of information can be distinguished by the difference in surface topography; third, true information can be decrypted using LSCM. Due to the bidirectional flow that can be precisely tuned, this robust and versatile approach not only paves the way for understanding the interaction between solvent and film surface with wettability gradient but also opens a door for applications in advanced anticounterfeiting.

Limitations of the study

Further studies are needed to explore what would happen if the micro/nanostructures produced using our method are heated at elevated temperatures. In particular, some improvement in materials design should be faced to avoid phase separation, and then larger feature height can be generated. Moreover, to further corroborate our findings, we will extend this approach to copolymer system including random and block copolymer. This will be an important step to show that our method can work in a broader field of applications.

STAR★METHODS

Detailed methods are provided in the online version of this paper and include the following:

- KEY RESOURCES TABLE
- RESOURCE AVAILABILITY
  - Lead contact
  - Materials availability
  - Data and code availability
- METHOD DETAILS
  - Preparation of the materials
  - Photomask fabrication
  - Fabrication of micro/nanostructures
  - Fabrication of samples for LSCM tests
  - Characterizations
- QUANTIFICATION AND STATISTICAL ANALYSIS

SUPPLEMENTAL INFORMATION

Supplemental information can be found online at https://doi.org/10.1016/j.isci.2024.108790.

ACKNOWLEDGMENTS

The authors are grateful for the financial support from the National Natural Science Foundation of China (grant nos. 52173066, 92156011, and 51921002). The authors would like to thank the Analysis and Testing Center in Peking University for technical support in characterizations.

AUTHOR CONTRIBUTIONS

H. Y. supervised the project. Y. J. and H. Y. designed the experiments. Y. J. performed the experiments. T. S., B. Y., and F. C. helped perform the experiments in Raman, AFM and POM. All authors discussed experiments and results. Y. J. wrote the original manuscript. T. S. and H. Y. revised the manuscript.

DECLARATION OF INTERESTS

All authors are co-inventors on a patent related to this work (No. CN202111434432.X).

Received: September 18, 2023
Revised: October 24, 2023
Accepted: January 2, 2024
Published: January 6, 2024

REFERENCES

1. Whitesides, G.M. (2006). The origins and the future of microfluidics. Nature *442*, 368–373.
2. Stone, H.A., Stroock, A.D., and Ajdari, A. (2004). Engineering flows in small devices: Microfluidics toward a lab-on-a-chip. Annu. Rev. Fluid Mech. *36*, 381–411.
3. Nistor, V., Cannell, J., Gregory, J., and Yeghiazarian, L. (2016). Stimuli-responsive cylindrical hydrogels mimic intestinal peristalsis to propel a solid object. Soft Matter *12*, 3582–3588.
4. Ijspeert, A.J. (2014). Biorobotics: Using robots to emulate and investigate agile locomotion. Science *346*, 196–203.
5. Gemmell, B.J., Colin, S.P., Costello, J.H., and Dabiri, J.O. (2015). Suction-based propulsion as a basis for efficient animal swimming. Nat. Commun. *6*, 8790.
6. Liu, L., Broer, D.J., and Onck, P.R. (2019). Travelling waves on photo-switchable patterned liquid crystal polymer films directed by rotating polarized light. Soft Matter *15*, 8040–8050.
7. Feng, W., Chu, L., de Rooij, M.B., Liu, D., and Broer, D.J. (2021). Photoswitching between water-tolerant adhesion and swift release by inverting liquid crystal fingerprint topography. Adv. Sci. *8*, 2004051.
8. Ryabchun, A., Lancia, F., and Katsonis, N. (2021). Light-fueled nanoscale surface waving in chiral liquid crystal networks. ACS Appl. Mater. Interfaces *13*, 4777–4784.
9. Liu, C., Sun, J., Li, J., Xiang, C., Che, L., Wang, Z., and Zhou, X. (2017). Long-range spontaneous droplet self-propulsion on wettability gradient surfaces. Sci. Rep. *7*, 7552.
10. De Jong, E., Wang, Y., Den Toonder, J.M.J., and Onck, P.R. (2019). Climbing droplets driven by mechanowetting on transverse waves. Sci. Adv. *5*, eaaw0914.
11. Sun, Q., Wang, D., Li, Y., Zhang, J., Ye, S., Cui, J., Chen, L., Wang, Z., Butt, H.J., Vollmer, D., and Deng, X. (2019). Surface charge printing for programmed droplet transport. Nat. Mater. *18*, 936–941.
12. Li, J., Zhou, X., Li, J., Che, L., Yao, J., McHale, G., Chaudhury, M.K., and Wang, Z. (2017). Topological liquid diode. Sci. Adv. *3*, eaao3530.
13. Li, C., Dai, H., Gao, C., Wang, T., Dong, Z., and Jiang, L. (2019). Bioinspired inner microstructured tube controlled capillary rise. Proc. Natl. Acad. Sci. USA *116*, 12704–12709.
14. Kumar, S. (2003). Deformation of soft elastomeric layers by periodic interfacial tension gradients. Langmuir *19*, 2473–2478.
15. Arshad, T.A., Kim, C.B., Prisco, N.A., Katzenstein, J.M., Janes, D.W., Bonnecaze, R.T., and Ellison, C.J. (2014). Precision Marangoni-driven patterning. Soft Matter *10*, 8043–8050.
16. Singer, J.P., Kooi, S.E., and Thomas, E.L. (2016). Focused laser-induced Marangoni dewetting for patterning polymer thin films. J. Polym. Sci. B Polym. Phys. *54*, 225–236.
17. Jones, A.R., Kim, C.B., Zhou, S.X., Ha, H., Katsumata, R., Blachut, G., Bonnecaze, R.T., and Ellison, C.J. (2017). Generating large thermally stable Marangoni-driven topography in polymer films by stabilizing the surface energy gradient. Macromolecules *50*, 4588–4596.
18. Cai, Z., Huang, Z., Li, Z., Su, M., Zhao, Z., Qin, F., Zhang, Z., Yang, J., and Song, Y. (2020). Evaporation induced spontaneous micro-vortexes through engineering of the Marangoni flow. Angew. Chem. Int. Ed. *59*, 23684–23689.
19. Shao, R., Meng, X., Shi, Z., Zhong, J., Cai, Z., Hu, J., Wang, X., Chen, G., Gao, S., Song, Y., and Ye, C. (2021). Marangoni flow manipulated concentric assembly of cellulose nanocrystals. Small Methods *5*, 2100690.
20. Abdollahi, A., Roghani-Mamaqani, H., Razavi, B., and Salami-Kalajahi, M. (2020). Photoluminescent and chromic nanomaterials for anticounterfeiting technologies: Recent advances and future challenges. ACS Nano *14*, 14417–14492.
21. Abdollahi, A., Roghani-Mamaqani, H., and Razavi, B. (2019). Stimuli-chromism of photoswitches in smart polymers: Recent advances and applications as chemosensors. Prog. Polym. Sci. *98*, 101149.
22. Abdollahi, A., Roghani-Mamaqani, H., Razavi, B., and Salami-Kalajahi, M. (2019). The light-controlling of temperature-responsivity in stimuli-responsive polymers. Polym. Chem. *10*, 5686–5720.
23. Abdollahi, A., Sahandi-Zangabad, K., and Roghani-Mamaqani, H. (2018). Rewritable anticounterfeiting polymer inks based on functionalized stimuli-responsive latex particles containing spiropyran photoswitches: Reversible photopatterning and security marking. ACS Appl. Mater. Interfaces *10*, 39279–39292.
24. Lei, Y., Dai, W., Guan, J., Guo, S., Ren, F., Zhou, Y., Shi, J., Tong, B., Cai, Z., Zheng, J., and Dong, Y. (2020). Wide-range color-tunable organic phosphorescence materials for printable and writable security inks. Angew. Chem. Int. Ed. *59*, 16054–16060.
25. Qin, L., Liu, X., He, K., Yu, G., Yuan, H., Xu, M., Li, F., and Yu, Y. (2021). Geminate labels programmed by two-tone microdroplets combining structural and fluorescent color. Nat. Commun. *12*, 699.
26. Zheng, Z., Hu, H., Zhang, Z., Liu, B., Li, M., Qu, D.-H., Tian, H., Zhu, W.-H., and Feringa, B.L. (2022). Digital photoprogramming of liquid-crystal superstructures featuring intrinsic chiral photoswitches. Nat. Photonics *16*, 226–234.
27. Zhou, H., Xue, C., Weis, P., Suzuki, Y., Huang, S., Koynov, K., Auernhammer, G.K., Berger, R., Butt, H.-J., and Wu, S. (2017). Photoswitching of glass transition temperatures of azobenzene-containing polymers induces reversible solid-to-liquid transitions. Nat. Chem. *9*, 145–151.
28. Yang, B., Cai, F., Huang, S., and Yu, H. (2020). Athermal and soft multi-nanopatterning of azopolymers: Phototunable mechanical properties. Angew. Chem. Int. Ed. *59*, 4035–4042.
29. Liu, Y., Liang, S., Yuan, C., Best, A., Kappl, M., Koynov, K., Butt, H.-J., and Wu, S. (2021). Fabrication of anticounterfeiting nanocomposites with multiple security features via integration of a photoresponsive polymer and upconverting nanoparticles. Adv. Funct. Mater. *31*, 2103908.
30. Xu, W.-C., Liu, C., Liang, S., Zhang, D., Liu, Y., and Wu, S. (2022). Designing rewritable dual-mode patterns using a stretchable photoresponsive polymer via orthogonal photopatterning. Adv. Mater. *34*, 2202150.
31. Katzenstein, J.M., Janes, D.W., Cushen, J.D., Hira, N.B., McGuffin, D.L., Prisco, N.A., and Ellison, C.J. (2012). Patterning by photochemically directing the Marangoni effect. ACS Macro Lett. *1*, 1150–1154.
32. Kim, C.B., Wistrom, J.C., Ha, H., Zhou, S.X., Katsumata, R., Jones, A.R., Janes, D.W., Miller, K.M., and Ellison, C.J. (2016). Marangoni instability driven surface relief grating in an azobenzene-containing polymer film. Macromolecules *49*, 7069–7076.
33. Kitamura, I., Oishi, K., Hara, M., Nagano, S., and Seki, T. (2019). Photoinitiated Marangoni flow morphing in a liquid crystalline polymer film directed by super-inkjet printing patterns. Sci. Rep. *9*, 2556.
34. Kitamura, I., Kato, K., Berk, R.B., Nakai, T., Hara, M., Nagano, S., and Seki, T. (2020). Photo-triggered large mass transport driven only by a photoresponsive surface skin layer. Sci. Rep. *10*, 12664.
35. Yu, H., and Ikeda, T. (2011). Photocontrollable liquid-crystalline actuators. Adv. Mater. *23*, 2149–2180.
36. Scriven, L.E., and Sternling, C.V. (1960). The Marangoni effects. Nature *187*, 186–188.
37. Sternling, C.V., and Scriven, L.E. (1959). Interfacial turbulence: Hydrodynamic instability and the Marangoni effect. AIChE J. *5*, 514–523.
38. Kim, C.B., Janes, D.W., Zhou, S.X., Dulaney, A.R., and Ellison, C.J. (2015). Bidirectional control of flow in thin polymer films by photochemically manipulating surface tension. Chem. Mater. *27*, 4538–4545.
39. Ichimura, K., Oh, S.-K., and Nakagawa, M. (2000). Light-driven motion of liquids on a photoresponsive surface. Science *288*, 1624–1626.
40. Lim, H.S., Han, J.T., Kwak, D., Jin, M., and Cho, K. (2006). Photoreversibly switchable superhydrophobic surface with erasable and rewritable pattern. J. Am. Chem. Soc. *128*, 14458–14459.
41. Kavokine, N., Anyfantakis, M., Morel, M., Rudiuk, S., Bickel, T., and Baigl, D. (2016). Light-driven transport of a liquid marble with and against surface flows. Angew. Chem. Int. Ed. *55*, 11183–11187.
42. Bird, J.C., Mandre, S., and Stone, H.A. (2008). Short-time dynamics of partial wetting. Phys. Rev. Lett. *100*, 234501.
43. Yang, B., Ji, Y., Cai, F., and Yu, H. (2023). Surface morphing of azopolymers toward advanced anticounterfeiting enabled by a two-step method: Light writing and then reading in liquid. ACS Appl. Mater. Interfaces *15*, 23804–23812.
44. Ubukata, T., Seki, T., and Ichimura, K. (2000). Surface relief gratings in host-guest supramolecular materials. Adv. Mater. *12*, 1675–1678.
45. Sokolowsky, K.P., Bailey, H.E., and Fayer, M.D. (2014). New divergent dynamics in the isotropic to nematic phase transition of liquid crystals measured with 2D IR vibrational echo spectroscopy. J. Chem. Phys. *141*, 194502.
46. Stuart, C.M., Frontiera, R.R., and Mathies, R.A. (2007). Excited-state structure and dynamics of cis- and trans-azobenzene from resonance Raman intensity analysis. J. Phys. Chem. A *111*, 12072–12080.
47. Song, T., Lei, H., Cai, F., Kang, Y., Yu, H., and Zhang, L. (2022). Supramolecular cation−π interaction enhances molecular solar thermal fuel. ACS Appl. Mater. Interfaces *14*, 1940–1949.
48. Bandara, H.M.D., and Burdette, S.C. (2012). Photoisomerization in different classes of azobenzene. Chem. Soc. Rev. *41*, 1809–1825.

49. Gaver, D.P., and Grotberg, J.B. (1990). The dynamics of a localized surfactant on a thin film. J. Fluid Mech. *213*, 127–148.
50. Jensen, O.E., and Grotberg, J.B. (1992). Insoluble surfactant spreading on a thin viscous film: shock evolution and film rupture. J. Fluid Mech. *240*, 259–288.
51. Chaudhury, M.K., and Whitesides, G.M. (1992). How to make water run uphill. Science *256*, 1539–1541.
52. Daniel, S., Chaudhury, M.K., and Chen, J.C. (2001). Past drop movements resulting from the phase change on a gradient surface. Science *291*, 633–636.
53. Pearson, J.R.A. (1958). On convection cells induced by surface tension. J. Fluid Mech. *4*, 489–500.
54. Haas, D.E., and Birnie III, D.P. (2002). Evaluation of thermocapillary driving forces in the development of striations during the spin coating process. J. Mater. Sci. *37*, 2109–2116.
55. Reichenbach, J., and Linde, H. (1981). Linear perturbation analysis of surface-tension-driven convection at a plane interface (Marangoni instability). J. Colloid Interface Sci. *84*, 433–443.
56. Weh, L. (1999). Self-organized structures at the surface of thin polymer films. Mater. Sci. Eng. C *8–9*, 463–467.
57. Yan, M., Tang, J., Xie, H.-L., Ni, B., Zhang, H.-L., and Chen, E.-Q. (2015). Self-healing and phase behavior of liquid crystalline elastomer based on a block copolymer constituted of a side-chain liquid crystalline polymer and a hydrogen bonding block. J. Mater. Chem. C *3*, 8526–8534.

STAR★METHODS

KEY RESOURCES TABLE

REAGENT or RESOURCE	SOURCE	IDENTIFIER
Chemicals, peptides, and recombinant proteins		
4-butylaniline	Aladdin	CAS: 104-13-2
Phenol	Sinopharm Chemical Reagents Beijing Co., Ltd	CAS: 108-95-2
6-chloro-1-hexanol	Aladdin	CAS: 2009-83-8
Triethylamine	Reagent depots of Peking University	CAS: 121-44-8
Methacryloyl chloride	Reagent depots of Peking University	CAS: 920-46-7
AIBN	Adamas	CAS: 78-67-1
5CB	Sinopharm Chemical Reagent, Beijing, China	CAS: 40817-08-1
Rhodamine 6G	Jiangsu Aikang Biomedical Research and Development Corporation	CAS: 989-38-8
Critical commercial assays		
Deuterated chloroform	Apres (Beijing) Technology Co., Ltd	CAS: 865-49-6
AFM microprobe	Bruker	https://www.brukersfmprobes.com
Silicon (Si) wafers	Zhejiang Lijing Silicon Material Corporation	CAS: 7440-21-3
Microsampler	Reagent depots of Peking University	Catalog No.: B2959
Deposited data		
Structure of PM6AZC4	This paper	https://pubs.rsc.org/en/content/articlelanding/2015/tc/c5tc01603g
Structure of 5CB	This paper	https://onlinelibrary.wiley.com/doi/epdf/10.1002/1521-4095%28200011%2912%3A22%3C1675%3A%3AAID-ADMA1675%3E3.0.CO%3B2-Z
Software and algorithms		
OriginLab Origin 2020b	OriginLab Corporation	https://www.originlab.com
Microsoft Excel	Microsoft	https://www.Microsoft.com
ChemDraw 19.1	PerkinElmer	https://www.perkinelmer.com/category/chemdraw
3ds Max 2017	Autodesk	https://www.autodesk.com.cn/products/3ds-max

RESOURCE AVAILABILITY

Lead contact

Further information and requests for resources and reagents should be directed to and will be fulfilled by the Lead Contact, Haifeng Yu (yuhaifeng@pku.edu.cn).

Materials availability

This study did not generate new unique reagents.

Data and code availability

All data reported in this paper will be shared by the lead contact upon request.

This paper does not report original code.

Any additional information required to reanalyze the data reported in this paper is available from the lead contact upon request.

METHOD DETAILS

Preparation of the materials

4-((4-butylphenyl)diazenyl)phenol was synthesized through the following steps: 4-butylaniline (10.0 g) was first dissolved in a mixture of water (116 mL) and HCl (24 mL) stirring at 0°C, then $NaNO_2$ (5.0 g) dissolved in water (100 mL) was added dropwise into the previous solution, then

the resulting solution was added dropwise into an aqueous solution of phenol (6.85 g) and NaOH (8.75 g) over a period of 2 h under magnetic stirring at 0°C. After that, HCl was added dropwise until pH = 3, finally the reaction solution was filtered and the crude product 4-((4-butylphenyl)diazenyl)phenol was obtained. 4-((4-butylphenyl)diazenyl)phenol (10.16 g), 6-chloro-1-hexanol (5.46 g), K_2CO_3 (5.52 g), KI (Traces) and DMF (100 mL) were added into a 500 mL flask with a magnetic stirring bar. The reaction mixture was heated to 130°C and reflux and stirred for 10 h. After cooling to room temperature, the crude product 6-(4-((4-butylphenyl) diazenyl)-phenoxy) hexanol was precipitated into cold water and collected by vacuum filtration. 6-(4-((4-butylphenyl) diazenyl)-phenoxy) hexanol (5.31 g) and triethylamine (3.03 g) were dissolved in dried THF (150 mL), then methacryloyl chloride (6 mL) dissolved in dried THF (50 mL) were added dropwise under magnetic stirring at 0°C for 24 h. Then solvent was removed under reduced pressure and crude product was obtained. Then the crude product was purified by column chromatography and recrystallized with methanol, finally 6-(4-((4-butylphenyl) diazenyl)-phenoxy) hexyl methacrylate (M6AZC4) was obtained. PM6AZC4 was synthesized by using the method of radical polymerization with liquid-crystalline monomer M6AZC4 and initiator AIBN.[57] First, M6AZC4 (2.2 g), AIBN (0.022 g) and anisole (4 mL) were added to a reaction tube. After being degassed with three freeze–thaw cycles, the tube was sealed in a nitrogen atmosphere. Then polymerization was carried out at 65°C for 24 h. Afterward, the reaction solution was diluted with THF and was then dripped into methanol. Finally, PM6AZC4 was obtained after precipitation from a large amount of methanol and was dried in a vacuum oven at 40°C for 24 h. 5CB was purchased from Sinopharm Chemical Reagent, Beijing, China, purity: 98%. Tetrahydrofuran (THF, Beijing Chemical Works) was distilled after drying with CaH_2 before use. Silicon (Si) wafers were purchased from Zhejiang Lijing Silicon Material Corporation. The thickness of the Si wafer was 500 μm. Rhodamine 6G was purchased from Jiangsu Aikang Biomedical Research and Development Corporation.

Photomask fabrication

The photomask of a periodic stripe and the photomasks consisting of transparent or opaque single stripes with different widths and other delicate patterns such as "PKU", four-leaf clover pattern, were designed through AutoCAD and fabricated by Shenzhen Micro/Nano Trading Corporation.

Fabrication of micro/nanostructures

The Silicon (Si) wafers and the photomasks were used as received. The polymer solution (PM6AZC4 in THF, 5 wt %) and small-molecular liquid-crystalline solution (5CB in THF, 5 wt %) were mixed together and well stirred to obtain the solution of mixture. Then the solution was spin-coated on the Si wafer (3000 rad min^{-1}, 30 s). After the solvent evaporation, the film was pre-illuminated with 365 nm UV (150 mW cm^{-2}, 60 s, distance between the sample and the light source: 7 cm) and then 530 nm green light (50 mW cm^{-2}, 60 s, distance between the sample and the light source: 5 cm). Subsequently, the film was patterned with a photomask using 365nm UV (150 mW cm^{-2}, 15 s, distance between the sample and the light source: 7 cm). Finally, the film was placed in a sealed container filled with solvent vapor for 45 min.

Fabrication of samples for LSCM tests

The Si wafer and the photomask containing "PKU" patterns were used as received. The polymer solution (PM6AZC4 in THF, 10 wt %) and small-molecular liquid-crystalline solution (5CB in THF, 10 wt %) were mixed together and well stirred to obtain the solution of mixture. Then added equal weight of fluorescent solution (Rhodamine 6G in THF, 0.02 wt %) into the previous solution and spin-coated on the Si wafer. Subsequently, the method of pre-illumination and UV-patterning was the same as before. Finally, the film was placed in a sealed container filled with ethanol vapor for 45 min.

Characterizations

^{1}H NMR spectra were recorded at room temperature on a Bruker-500 spectrometer using deuterated chloroform ($CDCl_3$) as the solvent with tetramethylsilane as an internal standard. The molecular weight of the polymer was characterized by gel permeation chromatography (Waters 1515) with a multi-angle light-scattering detector. THF was used as the eluent. Polarized optical microscopy (POM) was performed on a Zeiss Axio Scope A1 microscope with a Linkam LTSE420 hot stage. UV/Vis absorption spectra were recorded on a PerkinElmer Lambda-750 spectrophotometer. Differential scanning calorimetry (DSC) measurements were carried out on a PerkinElmer DSC 8000 instrument. Atomic force microscopy (AFM) images were obtained on a Bruker Icon instrument in a tapping mode (cantilever model: TESP-V2, Bruker). Contact-angle data were measured by Dataphysics Contact Angle Tester OCA-20. Fluorescent images and readout signal intensity mapping images were obtained using A1R-si Laser Scanning Confocal Microscope equipped with 561 nm laser and 580–620 nm detector. Raman measurements were performed on a DXRxi Micro Raman imaging spectrometer with 780 nm laser.

QUANTIFICATION AND STATISTICAL ANALYSIS

Data are represented as mean ± SEM. The analysis was carried out using Origin (OriginLab) and Excel tables.